Nanoscale

Non-Destructive Processing of Silver Containing Glass Ceramic Antibacterial Coating on Polymeric Surgical Mesh Surfaces

ARTICLE

Non-Destructive Processing of Silver Containing Glass Ceramic Antibacterial Coating on Polymeric Surgical Mesh Surfaces

Amin Zareei [a,b †], Venkat Kasi [a,b †], Allison Thornton [a,b], Ulisses Heredia Rivera [a,b], Sawale Manoj Ram Krishna [e], Murali Kannan Maruthamuthu [d], Zihao He [c], Juliane Nguyen [d], Haiyan Wang [a,c], Dharmendra Mishra [e], Rahim Rahimi [a, b,c*]

Surgical meshes composed of bioinert polymers such as polypropylene are widely used in millions of hernia repair procedures to prevent the recurrence of organ protrusion from the damaged abdominal wall. However, post-operative mesh infection remains a significant complication, elevating hernia recurrence risks from 3.6% to 10%, depending on the procedure type. While attempts have been made to mitigate these infection-related complications by using antibiotic coatings, the rise in antibiotic-resistant bacterial strains threatens their effectiveness. Bioactive glass-ceramics featuring noble metals, notably silver nanoparticles (AgNPs), have recently gained traction for their wide antibacterial properties and biocompatibility. Yet, conventional methods of synthesizing and coating of such materials often require high temperatures, thus making them impractical to be implemented on temperature-sensitive polymeric substrates. To circumvent this challenge, a unique approach has been explored to deposit these functional compounds onto temperature-sensitive polypropylene mesh (PP-M) surfaces. This approach is based on the recent advancements in cold atmospheric plasma (CAP) assisted deposition of SiO_2 thin films and laser surface treatment (LST), enabling the selective heating and formation of functional glass-ceramic compounds under atmospheric conditions. A systematic study was conducted to identify optimal LST conditions that resulted in the effective formation of a bioactive glass-ceramic structure without significantly altering the chemical and mechanical properties of the underlying PP-M (less than 1% change compared to the original properties). The developed coating with optimized processing conditions demonstrated high biocompatibility and persistent antibacterial properties (> 7 days) against both Gram-positive and Gram-negative bacteria. The developed process is expected to provide a new stepping stone towards depositing a wide range of functional bioceramic coatings onto different implant surfaces, thereby decreasing their risk of infection and associated complications.

Introduction

Hernia repair, a common surgical procedure addressing abdominal wall damage, often stems from various medical issues, including trauma, injury, or other conditions weakening the abdominal wall[1,2]. If left untreated, hernias can cause significant discomfort and severe pain, potentially leading to life-threatening complications such as blood flow obstruction and hernia strangulation[3]. More than one million abdominal hernia surgeries are performed annually in the US, costing up to $2.5 billion annually. Epidemiological data suggests that around 4% of the global population over 45 years of age suffers from inguinal hernia, with a consequent mortality rate of 7.5%[4,5].

In most hernia repair procedures, a synthetic mesh is used as a form of mechanical support to protect damaged muscles, ensuring the containment of organs within the abdominal wall and mitigating hernia reprojection[6]. Among various materials used in such meshes, polypropylene-based mesh (PP-M) structures are considered the most widely preferred material in hernia repairs due to their superior mechanical strength, chemical resistance, lightweight properties, and cost-effectiveness[7–9]. Despite these advantages, the risk of infection in PP-M is a leading cause of hernia repair failure, contributing to increased morbidity and mortality rates [10,11]. Infections post-hernia repair surgeries also result in significant healthcare expenditure due to hospital readmissions and reoperations [12–14].

Mesh infection generally involves a "race for the surface," where host cells and bacteria compete for adherence to the mesh surface[15,16]. If bacteria gain the upper hand, they rapidly form a biofilm resistant to both host defense mechanisms and antibiotics, necessitating the surgical removal of the infected mesh[17–19]. To mitigate these challenges, several preventive strategies have been developed, from antibiotic treatments to surface modifications and coatings of surgical meshes with metal nanoparticles[20–22]. Among these strategies, traditional

a. School of Materials Engineering, Purdue University, West Lafayette, IN 47907, USA
b. Birck Nanotechnology Canter, Purdue University, West Lafayette, IN 47907, USA
c. School of Electrical and Computer Engineering, Purdue University, West Lafayette, IN 47907, USA
d. Division of Pharmacoengineering and Molecular Pharmaceutics, Eshelman School of Pharmacy, University of North Carolina at Chapel Hill, Chapel Hill, NC 27599, USA
e. Department of Food Science, Purdue University, West Lafayette, IN 47907, USA
*rrahimi@purdue.edu
† Theses authors contributed equally

treatments using antibiotics, such as amoxicillin, ampicillin/sulbactam, and cefazolin, have long been recognized for their efficacy in inhibiting bacterial colonization and biofilm formation on implant surfaces, administered either locally or systemically [23–26]. However, their misuse can contribute to increased bacterial resistance, recurrence of infections, and potential toxicity to human tissues [27–29].

In addition to antibiotic-based strategies, modifying the surface of surgical meshes and applying coatings laden with metal nanoparticles, including silver, copper, and gold, have demonstrated exceptional efficacy in inhibiting bacterial adherence and biofilm formation [30,31]. Among these metals, silver has been widely used to augment antimicrobial functionality in various medical devices due to its broad spectrum of antibacterial activity against various pathogenic microorganisms [32]. While the precise antibacterial mechanism of silver remains an active area of research, it is generally understood that the antibacterial properties of this metal primarily arise from the dissolution of the metal surface and the oxidative stress induced by reactive oxygen species on the silver surface upon contact with biological fluids [33]. Owing to these unique properties, there has been considerable interest in applying silver in various forms as a coating for surgical mesh implants to mitigate infection risk. For instance, a study by Badiou et al. assessed the efficacy of silver-coated meshes against bacterial infection through in vitro and in vivo studies, demonstrating the significant antibacterial potential of silver-coated PP-M during animal hernia repair [34]. Zhang et al.

employed a composite material comprising polyethylene glycol (PEG), hydrogel containing AgNPs, and flexible polyurethane (PU) nanofibers to create surgical meshes with antibacterial properties, aimed at preventing post-hernia repair infections [35]. However, these approaches are constrained by silver's cytotoxic and genotoxic effects, characterized by the uncontrolled release of AgNPs into the bloodstream, which can result in tissue damage. Further, recent studies highlighting the cytotoxic impact of AgNPs have raised concerns about their use as an antibacterial agent in implantable devices, due to the severe adverse and toxic effects of silver compounds in their elemental form [36].

Despite the significant toxicity of silver in its elemental and ionic forms, recent studies examining immobilized structures of bioactive glass-ceramic compositions containing silver have revealed unique long-lasting antibacterial properties while maintaining a lower cytotoxicity profile [37–39]. In fact, recent research has demonstrated that silver-doped glass-ceramics not only exhibit bacteriostatic characteristics but also deliver rapid bactericidal action against Gram-positive and Gram-negative bacteria, such as *Escherichia coli* (*E. coli*) and *Staphylococcus aureus* (*S. aureus*) [40,41]. Moreover, prior studies have established that effectively trapping elemental silver within the highly cross-linked network of glass-ceramic structures enables controlled silver dissolution and the release of Ag^+ ions from the glass-ceramic. This mechanism results in increased and sustained antibacterial activity, alongside excellent biocompatibility [42]. Since their discovery, bioactive
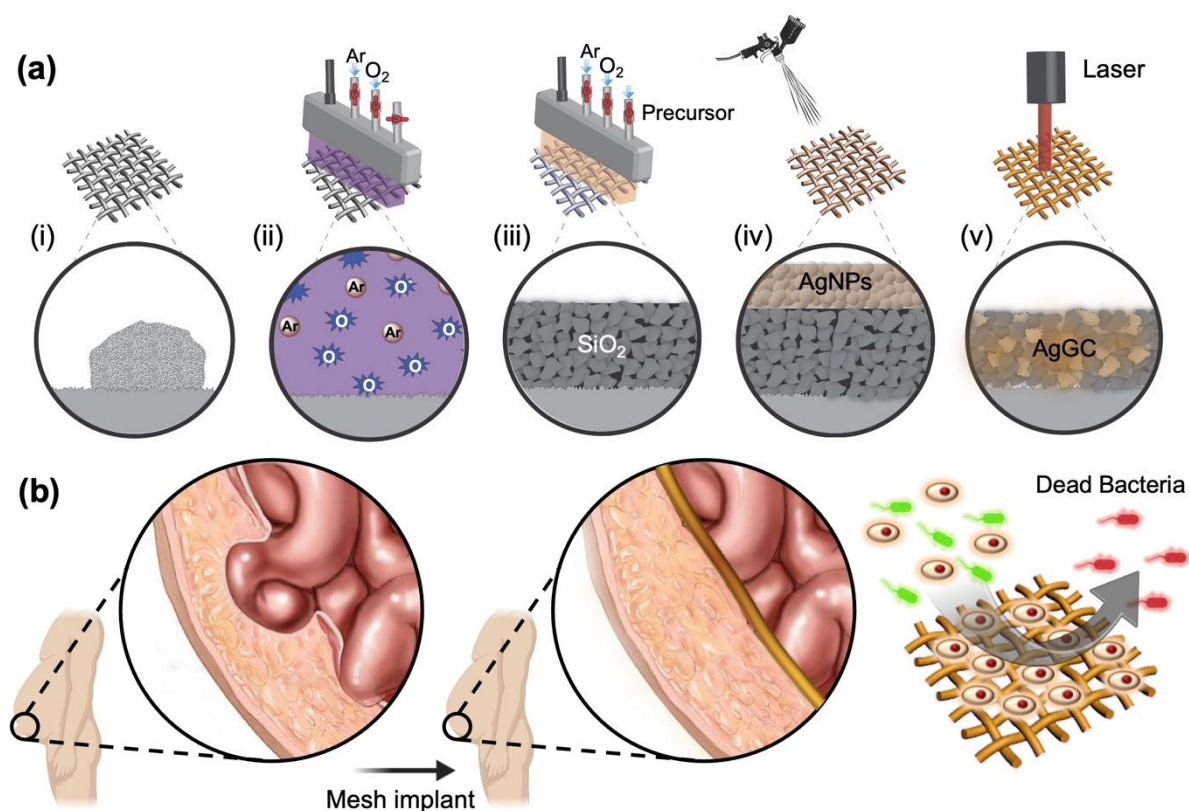
Figure 1. **(a)** Fabrication process of the AgGC coating on the surgical PP-M, **(i)** a pristine PP-M with contamination, **(ii)** oxygen plasma treatment to clean and functionalize the PP-M surface, **(iii)** CAP assisted SiO_2 deposition, **(iv)** AgNPs spray coating onto the SiO_2 coated PP-M surface, **(v)** LST and formation of AgGC coating on PP-M surface. **(b)** Implantation of the AgGC coated PP-M after hernia surgery with antibacterial properties.

glass-ceramics have been recognized as unique materials with the potential to serve as protective coatings for various medical implants. These materials have garnered considerable interest due to their beneficial properties, including high biocompatibility, robust mechanical strength, and resistance to corrosion[43–45]. Typically, glass-ceramics with antibacterial properties are synthesized by immobilizing noble metals such as silver within a silica coating, which is then subjected to heat treatment at temperatures reaching ~800 °C. This process allows for controlled nucleation and crystallization of the glass [46,47]. However, the high-temperature process conditions required for the synthesis of such coatings have restricted their application to ceramic and metallic surfaces.

To broaden the application of these coatings to temperature-sensitive PP-M substrates, we have investigated a novel approach that involves the selective deposition and formation of glass-ceramic coatings. This approach combines the utility of localized thin film deposition technologies with nondestructive heating processes, creating conditions suitable for fabricating these coatings on the desired substrates[48,49]. As illustrated in **Figure 1**, the process for creating a functional coating leverages the use of Cold Atmospheric Plasma (CAP) thin film deposition and spray coating technology. This allows us to selectively deposit the required SiO_2 and AgNPs, the active compounds for the glass-ceramic coating, onto the PP-M surface[50]. Subsequent laser surface treatment (LST) provides the essential selective and localized heating, leading to localized glass crystallization and, ultimately, the formation of elemental silver-containing glass-ceramic (AgGC).

In this work, a systematic study was conducted to determine the optimal coating and LST conditions for effectively forming AgGC coatings on PP-M surfaces with minimal thermal damage. A range of mechanical and material characterization studies were utilized for this investigation. In addition, the long-lasting antibacterial properties of the processed surfaces were examined against common strains of gram-positive and negative bacteria associated with hernia mesh related site infections. To ensure the safety of all materials and processes used in the coating procedure, the biocompatibility of the material coating under various laser processing conditions was validated in vitro using fibroblast cells.

Experimental Section

Materials

Knitted and undyed polypropylene meshes (with 800-micron pores) were purchased from Industrial Netting and were used as a mock surgical mesh throughout this study. The colloidal suspension of AgNPs with an average 60 nm particle size was purchased from Nova Centrix (JS-B25HV). 2,4,6,8-tetramethylcyclotetrasiloxane (TMCTS) (reagent grade) and phosphate-buffered saline (PBS) (Dulbeco's Phosphate Buffered Saline, pH 7.4) were obtained from Sigma Aldrich. All materials were used as received.

AgGC coating process

A cold atmospheric pressure plasma system (Atomflo 400D system, Surfx Technologies LLC, US) equipped with a 50-mm Linear Plasma Head was utilized for all surface modification and coating processes. This CAP System was operated with a capacitively coupled plasma source featuring a 27.12 MHz operating radio frequency. The plasma head was installed onto a three-axis robotic stage, allowing for precise positioning of the plasma head at a height of 5 mm above the surface to be treated and controlled scanning over the substrate during the surface treatment and deposition process. Scanning of the plasma head was performed at a rate of 1 m/min. The plasma glow within the plasma head was initiated using a mixture of primary and secondary plasma gas sources, regulated by a mass flow controller within the deposition system. The plasma gases comprised a primary gas of 30 L/min of high purity compressed argon (99.995%) and a secondary gas of 0.3 L/min of high purity compressed oxygen (99.999%).

As depicted in **Figure 1a**, the sequence of the deposition and surface modification process for the AgGC coating application onto the PP-M surface was as follows. The pristine PP-M surface was first cleaned to remove contamination and organic compounds. This was deemed necessary for enhancing adhesion and the subsequent attachment of coatings to the mesh substrate. This cleaning step involved treating both sides of the substrate with oxygen plasma (**Figure 1a (ii)**). Activated argon and oxygen atoms instigated a chemical reaction with organic contaminants on the mesh surface, resulting in the removal of these contaminants.

Following the plasma cleaning and surface activation process, a SiO_2 coating was applied onto the PP-M surface by introducing a silane precursor to the after-glow plasma region of the plasma head (**Figure 1a (iii)**). The TMCTS precursor was vaporized inside a bubbler at $T_V = 25$ °C and 7.1 Torr pressure by introducing argon gas at 1.5 L/min flow rate through the precursor liquid in the bubbler. The saturated argon gas carrying atomized TMCTS precursor was then passed through a tube connected to the plasma afterglow region of the plasma head. Here, the precursor molecules interacted with the plasma activated species, including reactive oxygen and UV radiation, leading to a localized chain polymerization reaction and deposition of SiO_2 directly onto the PP-M surface. This process was repeated on both sides of the PP-M. Subsequently, a colloidal suspension of AgNPs (2.5 wt% in water) was spray coated on both sides of the SiO_2-coated PP-M (**Figure 1a (iv)**). Post-spray coating, the mesh was placed in an oven for 10 min at 60 °C to ensure complete drying and solvent removal. Following this, the AgNPs and silica ($AgNPsSiO_2$) coated PP-M underwent local heat treatment using an Nd:YAG fiber laser (Universal Laser Systems, Inc., Scottsdale, AZ) with a 1.06 μm wavelength. To identify the optimum laser processing condition for effective localized heating and successful melting of the silver nanoparticles into the porous SiO_2 coating, thereby forming AgGC on the PP-M, a systematic study was carried out with different laser energy densities ranging from 15 J/cm^2 to 140 J/cm^2. This was done to find the optimal point providing the required thermal energy for AgGC coating formation, while minimizing damage to the underlying

mesh in terms of both chemical and physical properties (**Figure 1a (v)**). As shown in **Figure 1b**, the resultant AgGC coated PP-M mesh can be implanted not only to provide mechanical support to the damaged abdominal wall and prevent recurrence of hernia but also reduce post-operative infection related complications via antibacterial activity at the surgery site.

Material Characterization

In assessing the effective immobilization of AgNPs into the SiO_2 coating after different LST process conditions, a simple leaching test was performed. AgNPsSiO$_2$-coated PP-M samples were prepared as 1×1 cm rectangles and subjected to LST at varying energy densities from 15 J/cm^2 to 140 J/cm^2. Each uniquely treated sample was placed in a separate vial containing 100 ml of PBS to mimic physiological conditions and was incubated on an orbital shaker at 37 °C with 100 rpm for 48 h (MaxQ 4450, Thermo Fisher Scientific). The percentage of AgNPs leached from the mesh for each LST energy density was determined through absorption analysis, employing a calibration curve prepared by measuring the absorbance of known quantities of AgNPs with a multi-mode microplate reader (CLARIOstar Plus, BMG LABTECH).

Changes in the mechanical properties of the PP-Ms before and after LST at different energy densities were assessed using a universal testing machine (eXpert4000, Admet). All tensile tests were carried out on dog-bone-shaped specimens (length: 50 mm, gauge width: 3.2 mm) in accordance with the ASTM D638M standard, at a crosshead speed of 4 cm/min. Tensile experiments were performed in triplicate, and average elastic modulus and ultimate tensile strength were reported for each sample.

Morphological and elemental changes in the coatings on the PP-Ms before and after different LST processing conditions were observed using a scanning electron microscope (SEM) equipped with an energy-dispersive X-ray (EDS) detector (Hitachi-S 4800, Japan). Changes in thermal characteristics of the PP-Ms after different surface coating and processing conditions were investigated via thermogravimetric analysis (TGA) (TG 209 F3 Tarsus, Netzsch) and differential scanning calorimetry (DSC) (214 Polyma, Netzsch) at a heating rate of 20 °C/min.

The crystalline structures of the coatings on the PP-M surfaces following different processing conditions were analyzed by grazing incidence X-ray diffraction (GIXRD) using a PANalytical Empyrean multipurpose diffractometer (PANalytical, Almelo, The Netherlands) with a fixed Cu Kα anode (λ = 1.541, 87 Å) operating at 45 kV and 40 mA, and an incident beam angle fixed at ω = 2°. Surface chemical analysis of PP-Ms before and after various surface modification steps was conducted using attenuated total reflection Fourier-transform infrared (ATR-FTIR) (Nicolet Magna-IR Spectrometer 550 Series with an ATR accessory). Each spectrum was the averaged result of 10 scans collected in the wavenumber range of 700 cm-1 to 1400 cm^{-1} with a spectral resolution of 3 cm^{-1}.

The change in surface wettability of the PP-M surface after different surface modification steps was evaluated by water contact angle (WCA) measurements (Drop Shape Analyzer-DSA25, KRUSS). For all WCA measurements, a 5 µL DI water droplet was dispensed onto the mesh surface by an automatic dispensing unit, and the WCA was observed. Long-term wettability stability of each sample was analyzed by performing surface WCA measurements over 7 days. Each measurement was repeated 3 times on different sites on the mesh, with the average value being reported.

Antibacterial Evaluation and Stability Assessment

Cultures of Gram-negative pathogen *E. coli* (ATCC 43889) and Gram-positive pathogen MRSA (ATCC 43300) were grown for 24 h at 37 °C in an orbital shaker operating at 150 rpm. The *E. coli* was cultured in Luria Bertani (LB) broth, while MRSA was cultured in Tryptic soy broth (BD Difco NJ, USA). After the 24 h incubation period, the cultures were serially diluted and spread on selective media for bacterial enumeration. *E. coli* was plated on Sorbitol MacConkey Agar (SMAC) (BD Difco, NJ, USA), while MRSA was plated on Mannitol Salt Agar (MSA) (Oxoid, Basingstoke, UK). For the ensuing evaluations, the working volume of both bacterial cultures was adjusted to yield a concentration of 10^5 CFU/ml. The antibacterial efficacy of the prepared samples, including the control (pristine PP-M), AgNPsSiO$_2$-coated PP-M, and AgGC-coated PP-M, was assessed over a period of 7 days. The samples were cut into circular shapes with a diameter of 2 cm. On the first day, each sample was fully submerged in a suspension of either *E. coli* or MRSA (10^5 CFU/ml) and incubated at 37 °C for 24 h. Following the incubation, the culture medium was collected and spread on the respective selective agar plates, after which the viable bacterial colonies were enumerated. The samples were then cleaned using 80% isopropyl alcohol and re-immersed in fresh bacterial suspensions for another 24 h incubation period. This cycle of bacterial exposure, colony enumeration, cleaning, and re-exposure was carried out for 7 consecutive days. To ensure accuracy, all experiments were performed in triplicate, and the average CFU/ml value was calculated.

In vitro Biocompatibility Assessment

The in vitro biocompatibility of the modified PP-M was evaluated using NIH/3T3 fibroblast cells via two distinct assays: cell viability and live/dead immunostaining.

Cell Viability Assessment: The cytotoxicity of the prepared materials was analyzed using the CellTiter 96® Aqueous One assay (Promega), a colorimetric assay driven by enzyme activity. This assay measures cell viability through the metabolic activity of the cells. Only live cells possess the necessary enzymes, specifically ATP, to convert the assay's substrate into a spectrophotometrically detectable compound.

The NIH/3T3 cells were cultured in Dulbecco's Modified Eagle Medium: Nutrient Mixture F12 (DMEM/F12, Gibco) supplemented with 10% Fetal Bovine Serum (FBS) and 1% Penicillin/Streptomycin (Pen/Strep). A 12-well cell culture plate was seeded with a 200 µl cell

suspension, comprising DMEM/F-12 media (supplemented with 10% FBS and 1% Pen/Strep) and 5000 cells/ml. The pristine, AgNPsSiO₂-coated, and AgGC-coated PP-M samples, prepared as 2 cm diameter circles, were then introduced to the cell-seeded wells. The cells were then incubated at 37°C in a humidified 5% CO_2 atmosphere for 24 h. The culture was maintained for 1, 3, and 7 days.

Following each time period, the media was removed from the wells and replaced with 200 μl of MTT reagent. The samples with adhered NIH/3T3 cells were incubated for an additional hour, during which the cells metabolized the MTT reagent. Absorbance measurements were taken at 490 nm using a spectrophotometer (SpectraMax M2, Molecular Devices, USA) to assess the relative cell viability.

Live/Dead Immunostaining: The cell viability on the sample surfaces was further assessed through live/dead imaging. NIH/3T3 fibroblast cells were seeded at a standard concentration on the test specimens, and viability was assessed at 1, 3, and 7 days. Calcein-AM (0.2% (v/v)) and ethidium homodimer-1 (0.1% (v/v)) were used as the live and dead cell markers, respectively. Calcein-AM, metabolized by live cells to produce a fluorescent green compound, and ethidium homodimer-1, which enters dead cells and binds to nucleic acids, producing a red fluorescence, provided a visual contrast between live and dead cells. The fluorescence signals were captured using a fluorescence microscope (Nikon Ti2 Eclipse) with appropriate filters, and images were processed using NIS-Elements D software. This visual analysis of the cells on the surfaces of the modified meshes provided an additional level of evaluation regarding the biocompatibility of the surface modifications.

Results and Discussions

AgNP Leach test

The pursuit of sustained antibacterial properties was predicated on achieving robust adhesion of the AgNPs coating to the PP-M surface. The infusion of AgNPs via the LST process facilitated a potent bond within the SiO_2 coating. This potent adhesion was

crucial in curtailing the leaching of AgNPs from the mesh, thus reducing the potential for toxicity and infection upon implantation.

A comprehensive study was undertaken to discern the impact of LST energy density on the infusion quality of AgNPs into the SiO_2 coating. Experiments were conducted wherein the AgNPsSiO2-coated PP-Ms were subjected to varying LST energy densities. Following each LST iteration, the mesh was immersed in a PBS solution, and the percentage of leached AgNPs was quantified over a 48 h period. Pre-immersion optical images of the samples (**Figure 2a**) indicated a discernible color change from colorless (pristine PP-M) to silver (post-AgNPs spray coating process). Notably, LST application prompted a distinctive shift to a bright brown hue (**Figure 2a (iii-iv)**).

Upon optical inspection, it was observed that augmenting the laser energy density to 120 J/cm² incurred negligible alteration in the physical structure of the fibers and pore size on the meshes, with a change of less than 5%. However, further increase of laser energy density caused noticeable damage to the mesh structure and deformation of the PP-M fibers (**Figure 2a (iv)**).

Figure 2b exhibits AgNPsSiO₂-coated PP-M samples post-LST with varying laser energy densities, after the silver leaching experiment. Lower LST processing conditions (15 J/cm² energy density) showed complete leaching of AgNPs from the mesh surface, culminating in a clear color change in the test solution to black (**Figure 2b-c**).

In contrast, a clear reduction in AgNPs leaching from the mesh surface was observed upon incrementing the laser processing power, which also changed the PBS solution's color (**Figure 2c**). For AgNPsSiO₂-coated PP-M samples subjected to LST at 120 J/cm² energy density, the change in the solution color diminished to less than 1%. Even though a similar low AgNPs leaching behavior was observed for LST mesh samples processed at higher laser powers (140 J/cm²), the excessive
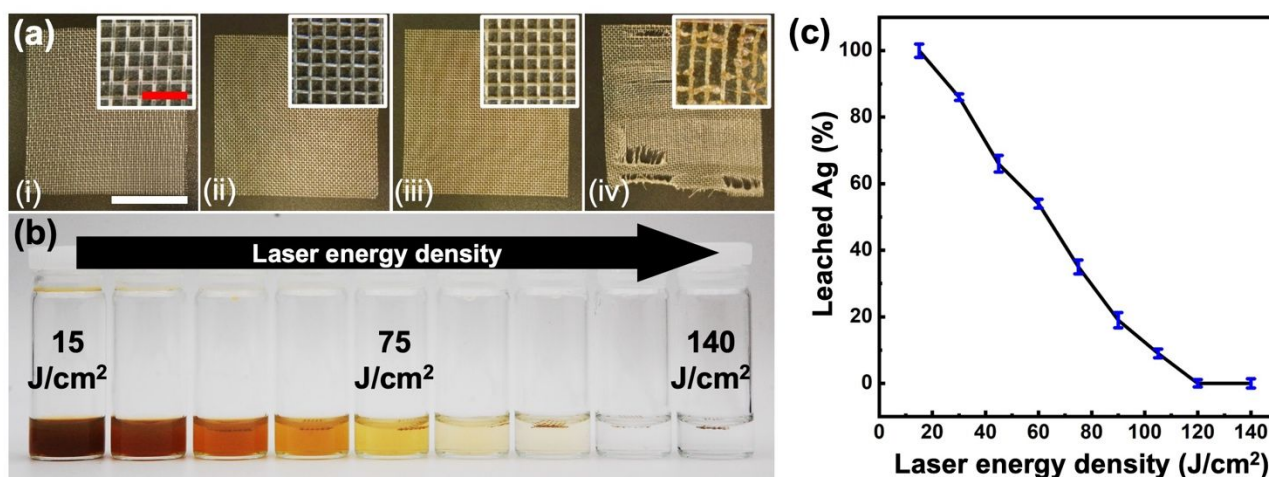
Figure 2. AgNPs leaching test from the PP-M surface before and after LST with different energy densities. **(a)** Microscopic images of **(i)** pristine PP-M, **(ii)** AgNPsSiO₂ coated PP-M before and after LST with **(iii)** 120 J/cm² and **(iv)** 140 J/cm² energy density. **(b)** Photographs of the immersed PP-M in PBS after LST with different energy densities . **(c)** Percentage of leached AgNPs from the PP-M surface after processing with different LST energy densities. (Red scale bar: 500 μm, white scale bar: 1.5 cm)
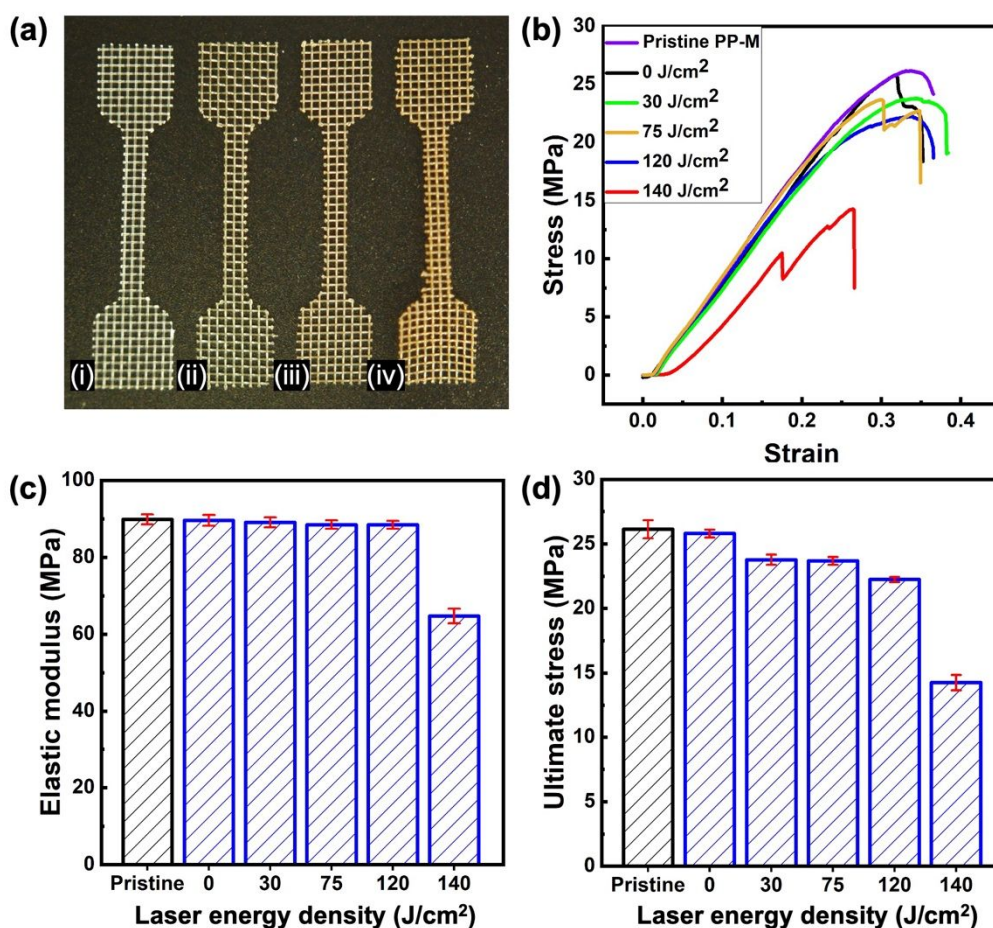
Figure 3. Mechanical characterization of PP-Ms before and after LST with different energy densities . **(a)** Photographs of samples for tensile tests, **(i)** pristine PP-M, **(ii)** AgNPsSiO$_2$ coated PP-M before LST, **(iii)** AgNPsSiO$_2$ coated PP-M after LST with 120 J/cm^2 energy density, **(iv)** AgNPsSiO$_2$ coated PP-M after LST with 140 J/cm^2 energy density. **(b)** Stress-strain curves of the pristine and AgNPsSiO$_2$ coated PP-Ms before and after LST with different energy densities. **(c)** Elastic modulus and **(d)** ultimate stress of the pristine and AgNPsSiO$_2$ coated PP-Ms before and after LST with different energy densities.

thermal energy inflicted conspicuous damage on the mesh fibers and caused burning (**Figure 2b-c**).

This led to the conclusion that the LST process provides localized and selective heating of AgNPs on the PP-M surface. When conducted at optimal energy levels, the laser-generated heat triggers melting of the AgNPs, which are then wicked into the nanoporous structure of the SiO$_2$ coating. The combined heating and silver infusion into SiO$_2$ segments induce local crystallization of the glass, ultimately forming a silver-containing glass ceramic (AgGC). Indeed, LST with adequate energies were found to yield reduced silver leaching from the coated PP-M surface, highlighting the beneficial effects of laser processing. However, caution must be exercised to prevent the application of excessive laser energies, as this could lead to unintended consequences including vaporization, material removal, and thermal damage to the underlying PP-M fibers. Balancing the need for robust silver nanoparticle adhesion and preserving the structural integrity of the fibers required careful adjustment of laser energy parameters. Therefore, optimizing the energy levels to both minimize silver leaching and avoid damage to the PP-M fibers was crucial to the successful application of this technique.

Mechanical characterization

In the realm of surgical interventions, meshes have been widely utilized for providing long-term reinforcement to compromised abdominal wall tissues following hernia repair surgery. It was thus critical to ensure that the surface modification process employed in this study did not adversely affect the mechanical properties of the PP-Ms.

In order to systematically assess this, a comprehensive evaluation of the mechanical properties of various samples was conducted. These samples included control pristine and AgNPsSiO$_2$ coated PP-Ms, both before and after the application of LST at different energy densities. The evaluation was based on tensile testing data (**Figure 3a-b**), from which the elastic modulus and ultimate tensile strength of the test samples were discerned for different processing conditions (**Figure 3c-d**).

Upon examining the results of these investigations, it was noted that the pristine PP-M exhibited an elastic modulus and ultimate tensile strength of approximately 89 MPa and 26 MPa respectively. A study of the influence of laser surface processing conditions revealed an interesting trend. In general, processing conditions with an energy density ≤ 120J/cm^2 led to minimal alterations in the mechanical properties of the processed PP-M,
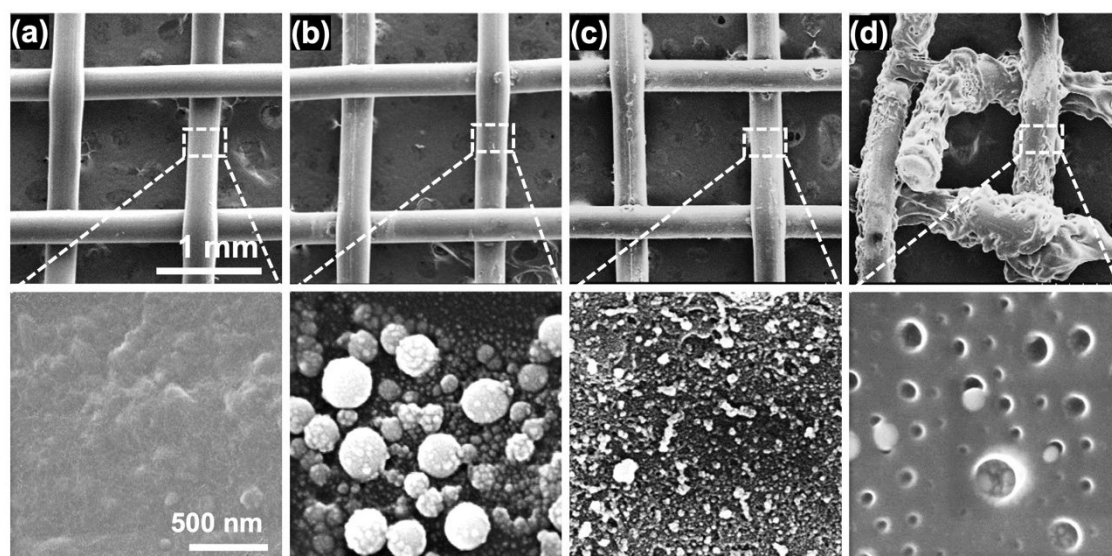
Figure 4. Surface SEM analysis. **(a)** Pristine PP-M, **(b)** AgNPsSiO$_2$ coated PP-M before LST, and AgNPsSiO$_2$ coated PP-M after LST with **(c)** 120 J/cm^2 and **(d)** 140 J/cm^2 energy density.

causing less than 2% and 9% changes in the overall elastic modulus and ultimate tensile strength respectively.

However, samples processed at higher laser energy densities ≥ 140 J/cm^2 demonstrated a clear deterioration in the mechanical properties of the processed PP-M. In these instances, a significant reduction, amounting to a 31% decrease in elastic modulus and a 52% decrease in ultimate tensile strength, was observed.

The implications of these findings underscored the need to carefully manage the energy density in the laser surface treatment to preserve the mechanical integrity of the PP-Ms while achieving the desired antimicrobial effects. Through the comprehensive leaching tests and mechanical characterizations, an energy density of 120 J/cm^2 was identified as the optimal condition for LST. Ensuring both sufficient adhesion of AgNPs and minimal compromise of mechanical properties, further investigations were conducted utilizing this optimized processing parameter.

Surface morphology and chemical characterization

Surface morphology of the pristine, AgNPsSiO$_2$ coated PP-Ms before and after LST was examined (**Figure 4**). The AgNPsSiO$_2$ coated PP-M exhibited the formation of AgNPs clusters up to 300 nm in size, which resulted from the aggregation of smaller nanoparticles (average size: 60 nm) post AgNPs spray coating and drying (**Figure 4a-b**). Upon subjecting to LST with the optimal energy density (120 J/cm^2), a uniform surface devoid of visible AgNPs clusters emerged, suggestive of AgNPs' infusion into the SiO$_2$ porous matrix on the PP-M fiber surface (**Figure 4c**). Notably, this processing condition did not noticeably alter the mesh fibers. Conversely, the application of higher laser energy density (140 J/cm^2) induced significant damage to the material microstructure, including void formation and mesh fiber deformation (**Figure 4d**). The occurrence of voids and large pores on the fibers could be ascribed to the PP vaporization during laser processing.

Cross-sectional SEM images of the pristine and AgNPsSiO$_2$ coated PP-Ms following optimal LST (energy density of 120 J/cm^2) are depicted in **Figure 5**. The coating on individual fibers appeared to be uniform and dense, exhibiting an average thickness of 1.12 μm on the PP-M fibers.

Elemental composition throughout the coating's thickness under optimal LST processing conditions (energy density of 120 J/cm^2) was investigated via EDS analysis (**Figure 6**).
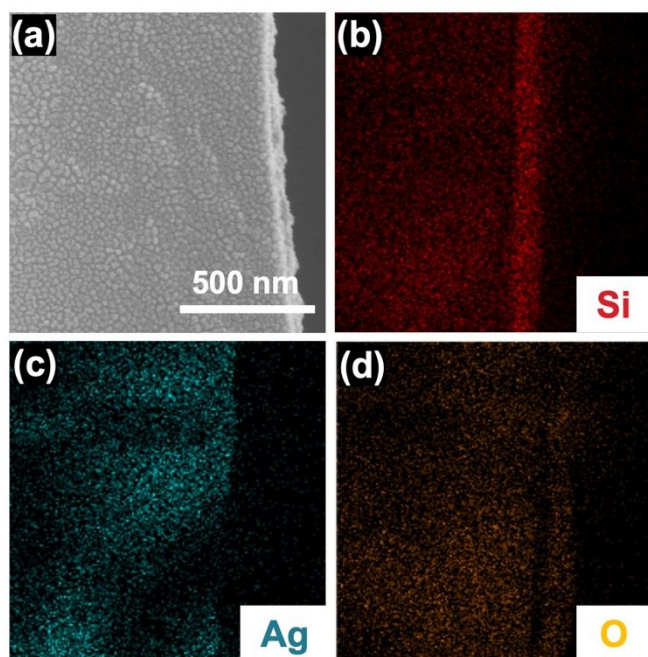
Figure 6. Cross-section EDS analysis of AgNPsSiO$_2$ coated PP-M after LST with 120 J/cm^2. (a) Cross-section SEM image, **(b)** corresponding elemental EDS mapping of **(b)** Si, **(c)** Ag, **(d)** O.

Figure 5. Cross-sectional SEM images. **(a)** Cross-section view of pristine PP-M, **(b)** high magnification view at the surface interface of single PP fiber, **(c)** cross-section view of AgNPsSiO$_2$ coated PP-M after LST with 120 J/cm^2, **(d)** high magnification view at the surface interface of single PP fiber after the AgNPsSiO$_2$ coating and LST with 120 J/cm^2.

The analysis revealed a uniform presence of Si and O elements, which originated from SiO$_2$ deposition through the CAP process. Moreover, the even through-thickness distribution of elemental Ag underscored the successful infusion of AgNPs into the SiO$_2$ porous matrix via LST. The AgNPs likely underwent significant temperature elevation rapidly due to absorption of the applied laser energy density (120 J/cm^2). This absorbed thermal energy could prompt the creation of a heat-affected zone surrounding the particles and subsequent heat transfer to the surrounding SiO$_2$ network. The imparted heat could potentially stimulate local crystallization in the SiO$_2$ network proximal to the infused AgNPs, culminating in the formation of an AgGC coating on the PP-M [51,52]. To further scrutinize this hypothesis, XRD analysis was conducted on AgNPsSiO$_2$ coated (without laser treatment) and AgGC coated PP-Ms (from this point onwards referred to as AgNPsSiO$_2$ coated PP-Ms subjected to LST using the optimal energy density of 120 J/cm^2) (**Figure 7a**).

The spectrum of AgNPsSiO$_2$ coated PP-M contains the characteristic peaks of Ag metal at 38°, 44°, and 78° diffraction angles corresponding to (111), (200), and (311) planes, respectively (JCPDS No. 04-0783). The spectrum of AgGC coated PP-M shows similar peaks with changes in intensity and sharpening. The change in intensity could be explained by the
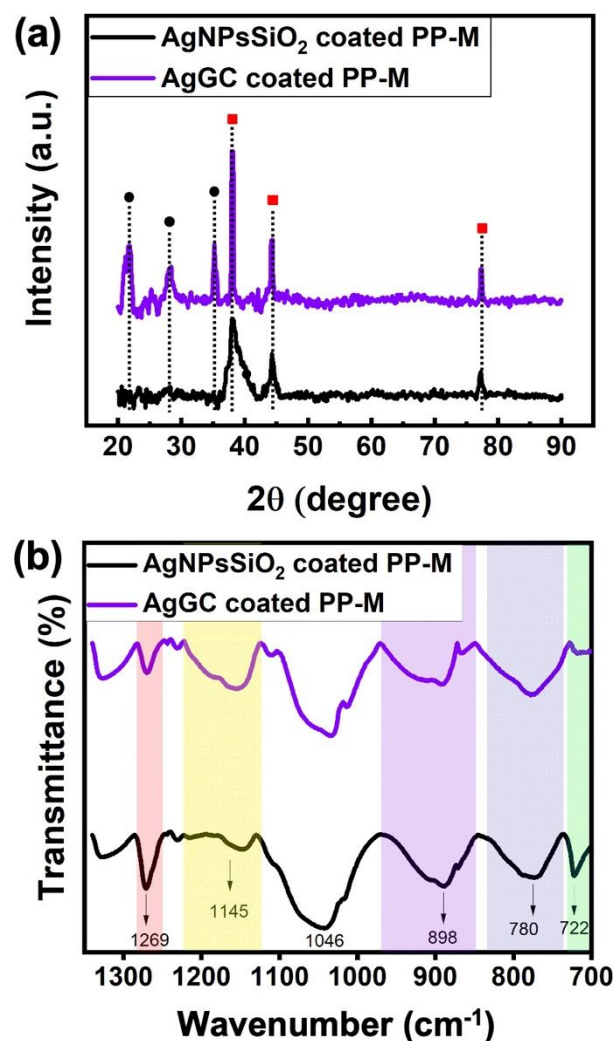
Figure 7. Physiochemical characterization. **(a)** GIXRD spectrum (Black circles: cristobalite, red squares: silver) and **(b)** FTIR spectrum of AgNPsSiO$_2$ coated PP-M before and after LST with 120 J/cm^2 (AgGC coated PP-M).
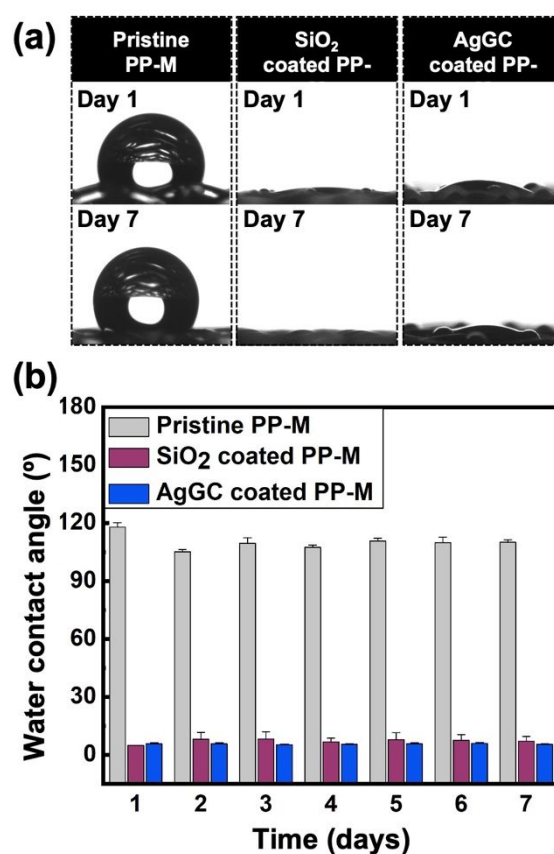
fact that LST enables the sintering and fusion of AgNPs, which results in an increase in the peak intensities. Further, Ag peak sharpening could be attributed to the entrapment of the AgNPs within the SiO$_2$ network, which is in agreement with previous findings[53]. Additionally, AgGC coated sample spectrum shows three newly formed peaks at 22°, 28°, and 35° diffraction angles corresponding to crystalline SiO$_2$, cristobalite (JCPDS No. 39-1425). This observation further confirms that the optimal LST on the AgNPsSiO$_2$ coated PP-M results in local crystallization in the AgNPs rich sites within the SiO$_2$ network and the formation of the AgGC coating onto the mesh surface [54,55]. To further investigate the surface chemistry and change in SiO$_2$ network structure due to the LST, ATR-FTIR analysis was performed on AgNPsSiO$_2$ coated and AgGC coated PP-Ms, as shown in **Figure 7b**. The FTIR spectrum of the AgNPsSiO$_2$ coated PP-M shows the existence of a symmetric -CH$_2$ vibration at 722 cm^{-1} and Si-CH$_3$ stretching at 1269 cm^{-1} due to the presence of carbon groups attached to silicon originating from the siloxane precursor
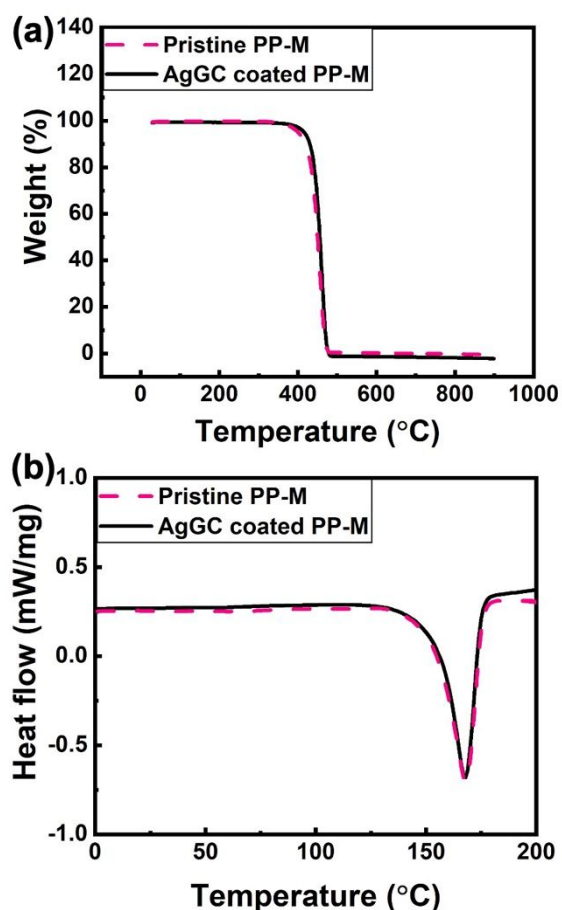
Figure 8. Thermal characterization of pristine PP-M and AgNPsSiO$_2$ coated PP-M after LST with 120 J/cm^2 (AgGC coated PP-M). **(a)** TGA and **(b)** DSC graph.

Figure 9. Water contact angle analysis of pristine, SiO$_2$ coated, and AgGC coated PP-Ms. **(a)** Optical images of water droplets on the surface of the mesh surface on day 1 and day 7. **(b)** Contact angle measurements as a function of time.

molecules [56]. Interestingly, the intensity of these two peaks decreased for the AgGC coated sample mainly because of the highly efficient heat transfer between the AgNPs and SiO$_2$ structure during the LST process that led to the reduction of carbon content in the SiO$_2$ structure. Both samples show the characteristic functional groups for SiO$_2$, such as asymmetric Si-O-Si stretching at 1046 cm^{-1}, Si-OH stretching at 898 cm^{-1}, and symmetric Si-O-Si stretching at 780 cm^{-1} [56]. In addition, a shoulder peak at 1145 cm^{-1} corresponding to asymmetric Si-O-Si stretching was observed in the spectra. It was found that the peak intensity of asymmetric Si-O-Si stretching at 1046 cm^{-1} remains nearly constant for both samples. Furthermore, the spectrum of the AgGC coated sample indicates that the peak intensity of Si-OH stretching decreased and the peak intensities of symmetric Si-O-Si stretching and asymmetric Si-O-Si stretching at 1145 cm^{-1} increased compared to that of AgNPsSiO$_2$ coated sample.
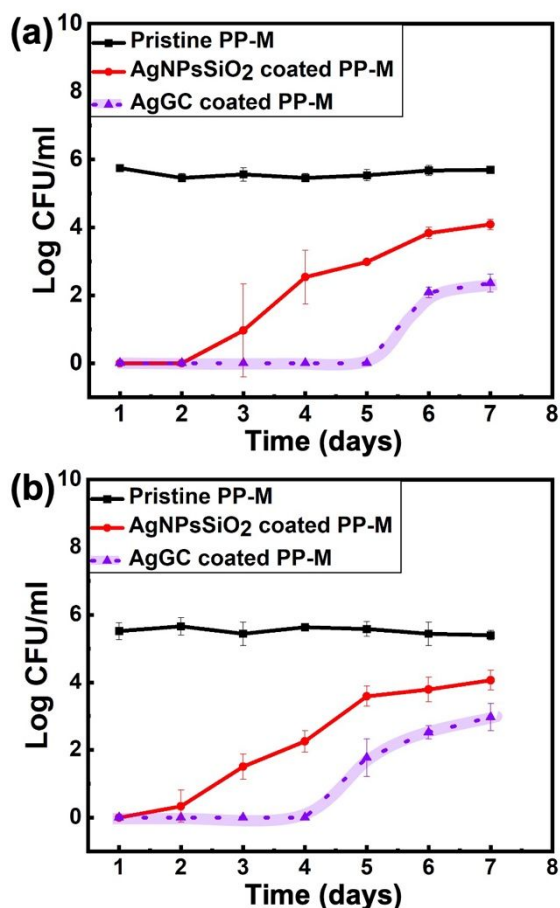
The reduction in the Si-OH stretching peak could be attributed to the condensation of silanol groups (Si-OH) forming more Si-O-Si linkages. This decrease was compensated by the increase in the peak intensities of symmetric Si-O-Si stretching and asymmetric Si-O-Si stretching at 1145 cm^{-1}. The experiment showed that while the peak intensity of asymmetric Si-O-Si stretching at 1046 cm^{-1} remained constant for either sample, the intensity of its shoulder

peak at 1145 cm^{-1} increased as a result of LST for the AgGC coated sample. The increase in the asymmetric Si-O-Si stretching shoulder peak after LST on the PP-M could be explained in terms of changes that occurred in the porous structure of the silica network related to transverse optical (TO) and longitudinal optical (LO) modes of the structure. It's been reported that mesoporous thin silica films exhibit different peak intensities for asymmetric Si-O-Si stretching at a lower frequency (1046 cm^{-1}) and higher frequency (1145 cm^{-1}) corresponding to TO and LO modes, respectively, depending on the degree of porosity in the films [57,58]. These studies suggest that an increase in wavenumbers and intensities of these two modes, especially LO mode, represents a decrease in the porosity of silica films and an increase in the inter tetrahedral bond angle and ring size of Si-O-Si, which might occur due to the formation of new Si-O-Si linkages from the condensation of Si-OH groups. The formation of new linkages could result in a less porous and tighter SiO$_2$ network. The obtained tight network after LST indicates effective entrapment of the AgNPs metal within the SiO$_2$ network.

To investigate the potential change in thermal behavior and degree of crystallinity in the PP-M with the LST process, DSC and TGA analysis were performed on the AgGC coated PP-M and compared to the pristine PP-M. **Figure 8a** shows TGA graphs of the samples. The thermal degradation temperature range of the pristine PP-M

Figure 10. Antibacterial property assessment of pristine PP-M and AgNPsSiO$_2$ coated PP-M before and after LST with 120 J/cm^2 (AgGC coated PP-M) for 7 days against **(a)** *E. coli* and **(b)** MRSA.

a similar behavior was obtained for the AgGC coated sample during the 7-day experiment, confirming its long-lasting hydrophilic surface properties.

Antibacterial characterization

The antibacterial characteristics of the pristine, AgNPsSiO$_2$ coated, and AgGC coated PP-Ms were assessed against Gram-negative E. coli and Gram-positive MRSA bacteria over a period of 7 days. As presented in **Figure 10**, the pristine PP-M demonstrated no discernible antibacterial properties. Although the AgNPsSiO$_2$ coated PP-M showed complete bacterial eradication against both E. coli and MRSA in the initial two days, it displayed a gradual decrease in antibacterial efficiency during the repeated antibacterial tests. For instance, against E. coli, a 4-log reduction was noted on the third day, which gradually diminished to a 2-log reduction by the seventh day (**Figure 10a**). A similar trajectory was observed against MRSA (**Figure 10b**), likely attributable to the gradual detachment of AgNPs from the AgNPsSiO$_2$ coated PP-M surface, leading to a decrease in its antibacterial properties over time.
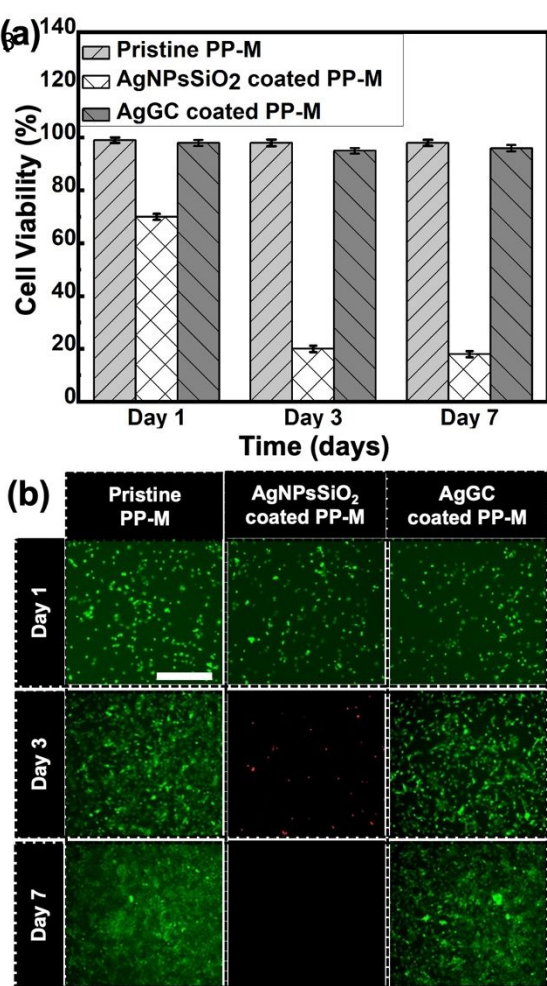
In contrast, the AgGC coated PP-M exhibited a notable enhancement in stable antibacterial characteristics, achieving complete eradication up to the fourth day, and maintaining over a 4-log reduction after seven days of antibacterial evaluation against both E. coli and MRSA. The observed sustained antibacterial effect for the AgGC coated samples is largely ascribed to the laser-induced entrapment of AgNPs within the glass ceramic matrix, thereby minimizing their leaching from the mesh surface.

Biocompatibility characterization

The biocompatibility of pristine, AgNPsSiO$_2$ coated, and AgGC coated PP-Ms was assessed using the MTT assay test. The samples were cultured with NIH 3T3 fibroblast cells over 1, 3, and 7 days (**Figure 11**). As shown in **Figure 11a**, the control group (pristine PP-M) exhibited no notable cytotoxicity towards the cells at the assessed intervals. In contrast, the AgNPsSiO$_2$ coated PP-M displayed a significant decline in cell viability to 18% by day 7. This observed cytotoxicity can be attributed to the leached AgNPs, which, at sufficient concentrations, can interfere with mitochondrial function by interacting with the electron transport system, thus instigating the formation of ROS, decreasing ATP levels, and ultimately initiating cell apoptosis.

Predictably, the AgGC coated sample demonstrated high cell compatibility. Observations revealed that this sample maintained biocompatibility throughout the 7-day experiment, with 96% viability on day 7, mirroring the control (Figure 11a). It is deduced that the glass ceramic network favorably impacts the retention of AgNPs on its surface, thereby minimizing silver release and cytotoxic effects. This evidence affirms that the fabricated AgGC coated PP-M is non-toxic to cells, indicating potential suitability for biomedical applications.

Additional confirmation of these results was obtained via a live-dead assay. Cells were stained with calcein-AM (live cells, green) and ethidium homodimer-1 (dead cells, red), and subsequently

(300-500 °C) remained unchanged after the LST process and formation of AgGC coating. **Figure 8b** shows DSC thermograms of the control pristine and AgGC coated PP-Ms. An endothermic peak at 165 °C was observed for the pristine sample, which is associated with the melting point of PP. A similar DSC curve was obtained for the AgGC coated PP-M with no change in the melting point. From this observation, it can be inferred that the degree of crystallinity of the PP-M remained unchanged after the complete AgGC coating process.

Sustained surface wettability is a key feature of many surgical meshes requiring direct contact and effective integration with the surrounding tissue. Furthermore, the improved surface wettability of surgical meshes with antibacterial coating agents can promote physical contact between the bacteria and the implant's surface, leading to enhanced bactericidal properties. Therefore, systematic static WCA measurements were performed to assess the effect and stability of the developed AgGC coating process. **Figure 9** demonstrates the WCA measurements for the pristine, SiO$_2$ coated, and AgGC coated PP-Ms for 7 days. The data shows that the SiO$_2$ coating rendered the surface of the mesh hydrophilic with a long-lasting effect over 7 days of measurements (θ < 10 °), which is attributed to the presence of silanol groups (Si-OH) in the SiO$_2$. Interestingly,

Figure 11. Biocompatibility investigation of pristine PP-M and AgNPsSiO$_2$ coated PP-M before and after LST with 120 J/cm^2 (AgGC coated PP-M). **(a)** Bar graph showing the relative cell viability percentage for pristine, AgNPSiO$_2$ coated, and AgGC coated PP-Ms with MTT assay. **(b)** Immunofluorescence images of NIH/3T3 fibroblast cells on days 1, 3, and 7 of cell culture along with test samples. NIH/3T3 fibroblast cells were stained with calcein and ethidium homodimer showing the live (green) and dead (red) cells (n=3) in three biological replicates. Pristine PP-M was considered as a control. Cell grown on control samples were considered 100% viable, and relative viability was calculated.

visualized with respective dyes to distinguish between live and dead cells. Microscopic fluorescence images, providing a merged view of both channels, were obtained on days 1, 3, and 7 of exposure (**Figure 11b**).

According to these observations, the control (pristine PP-M) demonstrated no toxic effect, with cells progressively growing over the 7-day period, illustrating the mesh material's compatibility. However, **Figure 11b** reveals a decrease in the number of living cells on the AgNPsSiO$_2$ coated PP-M over the 3 to 7-day interval. Furthermore, by days 3 and 7, a majority of the cells had detached from the plate and entered the culture media dead, presumably due to the leaching of AgNPs and resultant toxicity. In contrast, no dead cells were observed in the AgGC coated PP-M culture media over the 7-day period. This observation may be linked to the coating's capacity to effectively mimic the extracellular matrix, thereby promoting NIH-3T3 cell adhesion and proliferation over 7 days.

Conclusion

This study introduced a non-destructive approach for depositing AgGC coatings on surgical PP-Ms. The process incorporated CAP-assisted room-temperature SiO2 deposition and AgNPs dispersion spray coating onto the PP-M, followed by LST of the mesh surface. It was determined that a laser energy density of 120 J/cm^2 effectively facilitated the selective heating and infusion of AgNPs into the porous SiO2 network, which led to the crystallization and formation of a densely packed glass ceramic structure with infused silver elements, referred to as AgGC. This coating demonstrated sustained antibacterial efficacy against both E. coli and MRSA bacteria over a span of 7 days. Contrary to conventional processing techniques necessitating at least 1000 °C thermal energy for glass ceramic fabrication, this work introduces a novel research pathway to enable AgGC coating onto thermally sensitive polymeric substrates. This is envisioned to serve as a unique steppingstone towards the non-destructive and selective deposition of various functional glass ceramic coatings on diverse polymeric surfaces for medical device applications. Future work should focus on conducting systematic in vivo studies with animal models to can you confirm the safety and efficacy of the platform before its broader implementation in human applications.

Author Contributions

Amin Zareei: Methodology, Investigation, Visualization, Formal analysis, Writing – original draft, Writing –review & editing, Supervision, Validation, Investigation, **Venkat Kasi:** Methodology, Formal analysis, Writing – original draft, Writing–review & editing, Validation, **Allison Thornton:** Methodology, Formal analysis, **Ulisses Heredia Rivera:** Methodology, **Sawale Manoj Ram Krishna:** Methodology, Writing – original draft, Formal analysis, **Murali Kannan Maruthamuthu:** Methodology, Writing – original draft, Formal analysis, **Zihao He:** Methodology, **Juliane Nguyen:** Methodology, Writing – original draft, Formal analysis, **Haiyan Wang:** Methodology, **Dharmendra Mishra:** Methodology, Writing – original draft, Formal analysis, **Rahim Rahimi:** Conceptualization, Resources, Writing – review &editing, Supervision, Funding acquisition, Formal analysis, Project administration, Visualization

Conflicts of interest

There are no conflicts to declare.

Acknowledgements

References

1   C. Wang See, T. Kim and D. Zhu, *Engineered Regeneration*, 2020, **1**, 19–33.

2   W. W. Hope, W. S. Cobb and G. L. Adrales, *Textbook of Hernia*, 2017.

3   N. Dabbas, K. Adams, K. Pearson and G. Royle, *JRSM Short Reports*, 2011, **2**, 1–6.

4   K. Baylón, P. Rodríguez-Camarillo, A. Elías-Zúñiga, J. A. Díaz-Elizondo, R. Gilkerson and K. Lozano, *Membranes*, 2017, **7**, 1–23.

5   G. Muzio, M. Miola, S. Perero, M. Oraldi, M. Maggiora, S. Ferraris, E. Vernè, V. Festa, F. Festa, R. A. Canuto and M. Ferraris, *Surface and Coatings Technology*, 2017, **319**, 326–334.

6   B. Pérez-Köhler, Y. Bayon and J. M. Bellón, *Surgical Infections*, 2015, **17**, 124–137.

7   C. N. Brown and J. G. Finch, *Annals of the Royal College of Surgeons of England*, 2010, **92**, 272–278.

8   S. Kalaba, E. Gerhard, J. S. Winder, E. M. Pauli, R. S. Haluck and J. Yang, *Bioactive Materials*, 2016, **1**, 2–17.

9   F. Corduas, D. A. Lamprou and E. Mancuso, *Bio-Design and Manufacturing*, 2021, **4**, 278–310.

10   S. Mirel, A. Pusta, M. Moldovan and S. Moldovan, *Journal of Clinical Medicine*, 2022, 11.

11   L. He, X. Wang, G. Fan and Y. Zhao, *Frontiers in Surgery* , 2022, 9.

12   E. Furnée and E. Hazebroek, *Surgical Endoscopy*, 2013, **27**, 3998–4008.

13   C. A. Beadles, A. D. Meagher and A. G. Charles, *JAMA Surgery*, 2015, **150**, 194–200.

14   A. Roth, A. Krishnakumar and R. Rahimi, *FBE*, 2023, **15**, 9-null.

15   C. Kaoutzanis, S. W. Leichtle, N. J. Mouawad, K. B. Welch, R. M. Lampman, W. L. Wahl and R. K. Cleary, *Hernia*, 2015, **19**, 113–123.

16   H. J. Busscher, H. C. van der Mei, G. Subbiahdoss, P. C. Jutte, J. J. A. M. van den Dungen, S. A. J. Zaat, M. J. Schultz and D. W. Grainger, *Science Translational Medicine*, 2012, **4**, 153rv10-153rv10.

17   C. L. Romanò, H. Tsuchiya, I. Morelli, A. G. Battaglia and L. Drago, *Bone and Joint Research*, 2019, **8**, 199–206.

18   A. Roth, M. K. Maruthamuthu, S. Nejati, A. Krishnakumar, V. Selvamani, S. Sedaghat, J. Nguyen, M. N. Seleem and R. Rahimi, *Scientific Reports*, 2022, **12**, 13927.

19   S. Nejati, J. Wang, S. Sedaghat, N. K. Balog, A. M. Long, U. H. Rivera, V. Kasi, K. Park, J. S. Johnson, M. S. Verma and R. Rahimi, *Acta Biomaterialia*, 2022, **154**, 83–96.

20   A. M. Kao, M. R. Arnold, V. A. Augenstein and B. T. Heniford, *Plastic and Reconstructive Surgery*, 2018, **142**, 149S-155S.

21   L. He, X. Wang, G. Fan and Y. Zhao, *Frontiers in Surgery*, 2022, **9**, 1–8.

22   A. Krishnakumar, R. K. Mishra, S. Kadian, A. Zareei, U. H. Rivera and R. Rahimi, *Analytica Chimica Acta*, 2022, **1229**, 340332.

23   C. Labay, J. M. Canal, M. Modic, U. Cvelbar, M. Quiles, M. Armengol, M. A. Arbos, F. J. Gil and C. Canal, *Biomaterials*, 2015, **71**, 132–144.

24   I. Woodhouse, S. Nejati, V. Selvamani, H. Jiang, S. Chittiboyina, J. Grant, Z. Mutlu, J. Waimin, N. S. Abutaleb, M. N. Seleem and R. Rahimi, *ACS Applied Bio Materials*, 2021, **4**, 5405–5415.

25   S. Gopalakrishnan, S. Sedaghat, A. Krishnakumar, Z. He, H. Wang and R. Rahimi, *Advanced Electronic Materials*, 2022, **8**, 2101149.

26   V. Selvamani, S. Kadian, D. A. Detwiler, A. Zareei, I. Woodhouse, Z. Qi, S. Peana, A. M. Alcaraz, H. Wang and R. Rahimi, *Langmuir*, 2022, **38**, 4014–4027.

27   T. N. Robinson, J. H. Clarke, J. Schoen and M. D. Walsh, *Surgical Endoscopy and Other Interventional Techniques*, 2005, **19**, 1556–1560.

28   R. Narkhede, N. M. Shah, P. R. Dalal, C. Mangukia and S. Dholaria, *Indian Journal of Surgery*, 2015, **77**, 322–326.

29   U. Heredia-Rivera, S. Gopalakrishnan, S. Kadian, S. Nejati, V. Kasi and R. Rahimi, *Journal of Materials Chemistry C*, 2022, **10**, 9813–9822.

30   A. Zareei, V. Selvamani, S. Gopalakrishnan, S. Kadian, M. K. Maruthamuthu, Z. He, J. Nguyen, H. Wang and R. Rahimi, *Advanced Materials Technologies*, 2022, **7**, 2101722.

31   X. Saitaer, N. Sanbhal, Y. Qiao, Y. Li, J. Gao, G. Brochu, R. Guidoin, A. Khatri and L. Wang, *Coatings*, 2019, 9.

32   C. Marambio-Jones and E. M. V. Hoek, *Journal of Nanoparticle Research*, 2010, **12**, 1531–1551.

33   W. Sim, R. T. Barnard, M. A. T. Blaskovich and Z. M. Ziora, *Antibiotics*, 2018, **7**, 1–15.

34   W. Badiou, J. P. Lavigne, P. J. Bousquet, D. O'Callaghan, P. Marès and R. De Tayrac, *International Urogynecology Journal*, 2011, **22**, 265–272.

35   S. Zhang, K. Xu, L. Ge, M. A. Darabi, F. Xie, S. Derakhshanfar, Y. Liu, M. M. Q. Xing and H. Wei, *RSC Advances*, 2016, **6**, 90571–90578.

36   A. Almatroudi, H. Khadri, M. Azam, A. H. Rahmani, F. K. Al Khaleefah, R. Khateef, M. A. Ansari and K. S. Allemailem, *Processes*, 2020, 8.

37   J. J. Blaker, S. N. Nazhat and A. R. Boccaccini, *Biomaterials*, 2004, **25**, 1319–1329.

38   A. C. Marsh, N. P. Mellott, N. Pajares-Chamorro, M. Crimp, A. Wren, N. D. Hammer and X. Chatzistavrou, *Bioactive Materials*, 2019, **4**, 215–223.

39   J. S. Fernandes, P. Gentile, R. A. Pires, R. L. Reis and P. V. Hatton, *Acta Biomaterialia*, 2017, **59**, 2–11.

40   N. Pajares-Chamorro, J. Shook, N. D. Hammer and X. Chatzistavrou, *Acta Biomaterialia*, 2019, **96**, 537–546.

41   H. Zhu, C. Hu, F. Zhang, X. Feng, J. Li, T. Liu, J. Chen and J. Zhang, *Materials Science and Engineering: C*, 2014, **42**, 22–30.

42   M. Bellantone, N. J. Coleman and L. L. Hench, *Journal of Biomedical Materials Research*, 2000, **51**, 484–490.

43   G. Wang, Z. Lu, X. Liu, X. Zhou, C. Ding and H. Zreiqat,

Journal of the Royal Society Interface, 2011, **8**, 1192–1203.

44 M. Chen, W. Li, M. Shen, S. Zhu and F. Wang, *Corrosion Science*, 2013, **74**, 178–186.

45 A. Majumdar and S. Jana, *Bulletin of Materials Science*, 2001, **24**, 69–77.

46 R. D. Rawlings, J. P. Wu and A. R. Boccaccini, *Journal of Materials Science*, 2006, **41**, 733–761.

47 M. S. Shekhawat, *International Journal of Materials Physics*, 2015, **6**, 1–6.

48 U. Heredia-Rivera, V. Kasi, A. Krishnakumar, S. Kadian, A. K. Barui, Z. He, H. Wang, L. Stanciu and R. Rahimi, *ACS Applied Materials & Interfaces*, 2023, **15**, 17078–17090.

49 S. Sedaghat, V. Kasi, S. Nejati, A. Krishnakumar and R. Rahimi, *Journal of Materials Chemistry C*, 2022, **10**, 10562–10573.

50 V. Kasi, S. Sedaghat, A. M. Alcaraz, M. K. Maruthamuthu, U. Heredia-Rivera, S. Nejati, J. Nguyen and R. Rahimi, *ACS Applied Materials and Interfaces*, 2022, **14**, 9697–9710.

51 P. Merkl, S. Zhou, A. Zaganiaris, M. Shahata, A. Eleftheraki, T. Thersleff and G. A. Sotiriou, *ACS Applied Nano Materials*, 2021, **4**, 5330–5339.

52 T. M. Gross, J. Lahiri, A. Golas, J. Luo, F. Verrier, J. L. Kurzejewski, D. E. Baker, J. Wang, P. F. Novak and M. J. Snyder, *Nature Communications*, 2019, **10**, 1–8.

53 K. S. Moon, H. Dong, R. Maric, S. Pothukuchi, A. Hunt, Y. I. Li and C. P. Wong, *Journal of Electronic Materials*, 2005, **34**, 168–175.

54 M. G. Garníca-Romo, J. González-Hernández, M. A. Hernández-Landaverde, Y. V. Vorobiev, F. Ruiz and J. R. Martínez, *Journal of Materials Research*, 2001, **16**, 2007–2012.

55 A. C. C. Rotzetter, N. A. Luechinger, E. K. Athanassiou, D. Mohn, F. M. Koehler and R. N. Grass, *Journal of Materials Chemistry*, 2010, 7769–7775.

56 D. L. Wood and E. M. Rabinovich, *Applied Spectroscopy*, 1989, **43**, 263–267.

57 S. L. Warring, D. A. Beattie and A. J. McQuillan, *Langmuir*, 2016, **32**, 1568–1576.

58 P. Innocenzi, *Journal of Non-Crystalline Solids*, 2003, **316**, 309–319.